Journal of the Korean Ceramic Society (2020) 57:24–39
https://doi.org/10.1007/s43207-019-00003-1

REVIEW ARTICLE

Recent advances in ABO_3 perovskites: their gas-sensing performance as resistive-type gas sensors

Peresi Majura Bulemo[1,2] · Il-Doo Kim[1,3]

Received: 7 August 2019 / Revised: 4 October 2019 / Accepted: 7 October 2019 / Published online: 16 December 2019

Abstract
Perovskite-type oxides with general stoichiometry ABO_3 (A is a lanthanide or alkali earth metal, and B is transition metal) constitute a rich material playground for application as resistive-type gas-sensing layers. Immense interest is triggered by, among other factors, stability of abundant elements (≈90% in the periodic table) in this stoichiometry, relatively easy tunability of structure and chemical composition, and their off-stoichiometry stability upon doping. Moreover, their capability to host cationic and abundant oxygen vacancies renders them with excellent electrical and redox properties, and synergistic functions that influence their performance. Herein, we present an overview of recent development in the use of ABO_3 perovskites as resistive-type gas sensors, clearly elucidating current experimental strategies, and sensing mechanisms involved in realization of enhanced sensing performance. Finally, we provide a brief overview of limitations that hamper their potential utilization in gas sensors and suggest new pathways for novel applications of ABO_3 materials.

Keywords Perovskites · Sensors · Doping · Oxygen vacancies · Porosity

1 Introduction

Tailor-made ternary oxide bearing gas-sensing functionalities constitute a rich material playground for realization of enhanced gas sensing in resistive-type gas sensors. Among them, perovskite oxides remain prominent, and exhibit a wide range of physico-chemical properties, and tunable electronic conductivity compared to binary metal oxides such as SnO_2, ZnO, CuO, Co_3O_4, NiO, TiO_2, CeO_2, and WO_3. Perovskite oxides with the stoichiometry ABO_3 have a cubic structure (Fig. 1a, b), where the larger cation A at each corner of a unit cell and the smaller cation B at the body center sites are 12- and 6-fold coordinated with oxygen anions at the face center sites, respectively [1–3]. The sizes of A and B are determined by the tolerance factor, whose value equals unity for perfectly matched A–O and B–O-bond lengths [4]. Typically, the A-site cation at the dodecahedral site donates electrons to the $[BO_6]$ octahedra, whereas the B-site cation alters the electronic structure, influencing the physical properties of the perovskite oxide. Owing to the presence of oxygen vacancies, the stoichiometry of oxygen in ABO_3 perovskites deviates from 3, forming $ABO_{3-\delta}$ perovskite oxides with oxygen nonstoichiometry (δ). In vacancy-rich regions, hoping of oxygen-ion vacancies can mediate the diffusion of oxygen on the $[BO_6]$ octahedra, with energy barrier as low as 0.12 eV (Fig. 1c) [5, 6]. These oxygen vacancies act as centers of positive charges, and correlate linearly with hole density, whose increase results in high conductivity [7].

ABO_3 perovskites have been considered as promising resistive-type gas sensors because of (1) stability of abundant metallic elements in the ABO_3 perovskite structure [2], (2) tunability of structure and chemical composition upon partial substitution of A and/or B positions with aliovalent elements of various sizes and valences [8], (3) adaptability of structural integrity under off-stoichiometry [9], and (4) remarkable electronic structure and electron mobility [10]. As interstitial oxygen in a perovskite structure is thermodynamically unfavored, oxygen-deficient vacancies are

✉ Il-Doo Kim
idkim@kaist.ac.kr

1 Department of Materials Science and Engineering, Korea Advanced Institute of Science and Technology (KAIST), 291 Daehak-ro, Yuseong-gu, Daejeon 34141, Republic of Korea

2 Department of Mechanical and Industrial Engineering, University of Dar es Salaam, P. O. Box 35131, Dar es Salaam, Tanzania

3 Advanced Nanosensor Research Center, KI Nanocentury, KAIST, 291 Daehak-ro, Yuseong-gu, Daejeon 34141, Republic of Korea

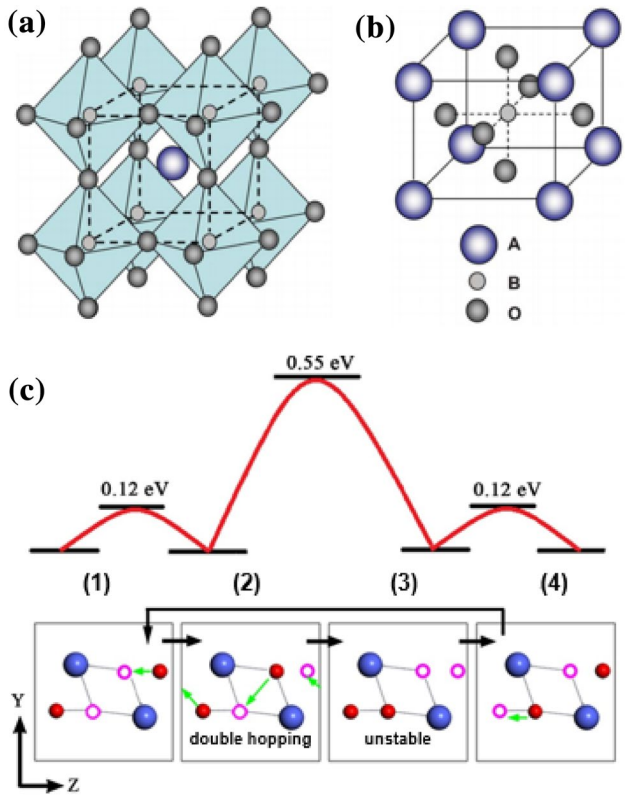

Fig. 1 Schematic of perovskite ABO_3 structure showing **a** corner-sharing (BO_6) octahedra with A ions located in 12-coordinated interstices, and **b** B-site cation at the center of the cell (Reproduced from Ref. [3]. with permission from The Royal Society of Chemistry). **c** Oxygen diffusion pathway (green arrows) in lanthanum cobaltite [$LaCoO_{3-\delta}$] (bottom) with the corresponding energy barriers (top). Open pink circles stand for O vacancies, whereas big blue and small red spheres stand for Co and oxygen atoms, respectively. Oxygen begins with hoping to a neighboring vacancy through space between Co atoms [1, 2] to form oxygen pair [3]. The O–O pair is unstable in absence of vacancies, forcing one atom to advance to the next vacancy, while the other jumps to initial position [4] (Ref. [5])—reprinted with permission from Elsevier

dominant and typically quite common compared to cationic vacancies. This is possibly due to the fact that anionic vacancies require small energy than cationic counterparts [11]. The ability to host cationic and oxygen vacancies renders ABO_3 perovskites with variable electrical and redox properties, synergistic catalytic functions, which bring about critical impact on gas-sensing property. In addition, their mechanical and thermal stability make them suitable gas-sensing materials in a wide range of temperatures. However, there are several issues to address. These include (1) metastability and likelihood to decompose into mixed oxide phases in low/high-temperature regimes [11–13], (2) proneness to moisture uptake by oxygen vacancies and consequent mobility of hydroxyl groups that pose cross sensitivity to moisture [14–16], and (3) massive variation of oxygen vacancy concentration with temperature and oxygen partial pressure, limiting oxygen adsorption [17]. In principle, improvement of perovskite oxides to suit desired performance involves tailoring their functional characteristics through strain induction [9, 18], inductive effects [19], doping [20, 21], and tunability of chemical composition [8].

Herein, we present an overview of recent development in the use of ABO_3 perovskites as resistive-type gas sensors, clearly elucidating current experimental methods, and strategies employed to realize sensing performance enhancements. Finally, we include a summary of sensing performance and an overview of obstacles that hinder their utilization as gas sensors, and suggest new pathways for novel applications.

2 ABO_3 perovskite oxides

In general, tunability of structural composition of ABO_3 perovskites depends on oxidation states of A and B cations [22]. These oxides can be *p*-type or *n*-type semiconducting oxides [23, 24]. Typically, occupancy of A and B sites with trivalent cations of rare-earth metals makes ABO_3 perovskites *p*-type conductors, with electron holes and cationic vacancies constituting the majority of nonstoichiometric defects. Accordingly, the number of oxygen vacancies in *p*-type ABO_3 perovskites is substantially low, as they are not the native nonstoichiometry defects [25]. Early investigations on ABO_3 perovskites show that they exhibit remarkable conductivity, redox properties, and reversibility in air/gas ambient [26]. To date, several investigations have emerged, further elucidating their interaction mechanisms with air/gas [27], synthesis and morphology engineering techniques [28], temperature dependency and sensing stability [28, 29], humidity effects [30], and response/recovery kinetics [31]. Particularly, some *p*-type ABO_3 perovskites such as $LaFeO_3$ have been the focus of investigations [7, 32–36]. Their high-temperature stability, nonstoichiometric composition as well as ionic and electronic conductivity make them important material for gas-sensing applications. One of the interesting works is that of Queralto et al. [29], who demonstrated a unique interaction of lanthanum ferrite ($LaFeO_3$) with sulfur containing gases (SO_2 and H_2S). In their study, they used electrospun $LaFeO_3$ nanofibers (NFs) as sensing materials (Fig. 2a, b). As illustrated in Fig. 2c, SO_2 strongly binds on $LaFeO_3$, leading to the formation of $La_2(SO_4)_3$, as lanthanum cations are Lewis acids and capable of adopting higher coordination numbers than iron (Fe). The results of their study showed that optimal sensing toward 1 ppm of SO_2 could be obtained at 250 °C, indicating a sensitivity $[(R_g - R_a)/R_a \times 100\%]$ as high as 90% (Fig. 2d). Despite this performance, SO_2 reacted with H_2O to yield sulfurous acid or bisulfite ion instead, leading to slow response/recovery of $LaFeO_3$. This indicates that humidity can have a serious effect on gas-sensing performance of $LaFeO_3$. In addition,

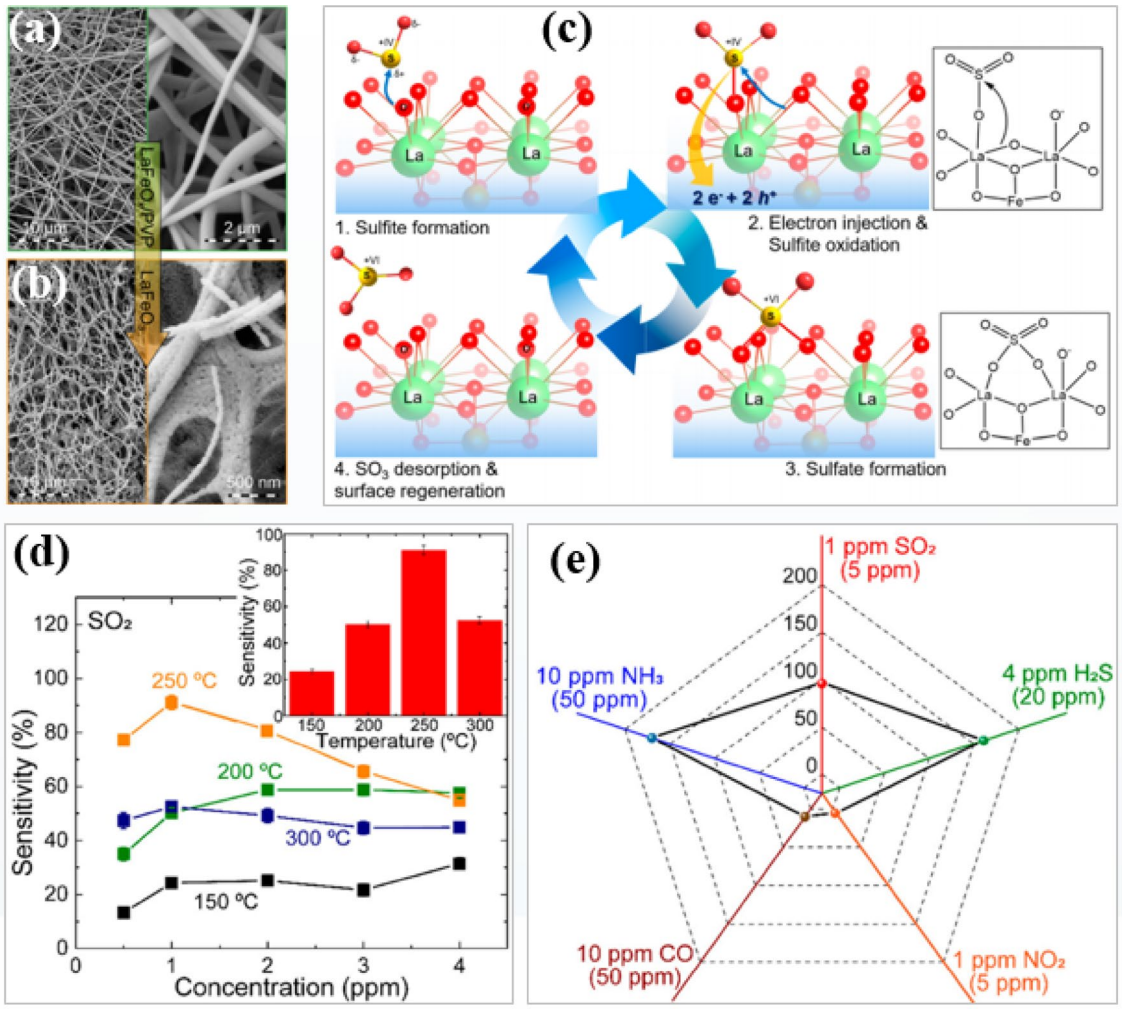

Fig. 2 SEM micrographs showing **a** as-spun $LaFeO_x$/PVP nanofibers and **b** $LaFeO_3$ nanofibers after calcination at 600 °C for 5 h with a ramping rate of 1 °C min^{-1} in the air. **c** Reaction mechanism of SO_2 to sulfate species with $LaFeO_3$ nanofibers and the desorbed SO_3, **d** variation of sensitivity $[(R_g\_R_a)/R_a \times 100\%]$ of $LaFeO_3$ with concentration of SO_2. The inset shows the dependence of sensitivity on operating temperature upon exposure to 1 ppm of SO_2. **e** Sensitivity of $LaFeO_3$ for 1 ppm of SO_2, 4 ppm of H_2S, 1 ppm of NO_2, 10 ppm of NH_3, and 10 ppm of CO measured at 250 °C (Reprinted with permission from Ref. [29]). Copyright (2019) American Chemical Society]

the gas responses of $LaFeO_3$ to NH_3 and H_2S remained high, indicating that the presence of these gases can interfere SO_2 sensing (Fig. 2e). Typically, incorporation of physical/chemical filters on sensing layers [37], or catalysts such as CeO_2 [38, 39], can reduce deleterious humidity effects and interfering gases. Recently, Ma et al. introduced a humidity-independent NH_3 sensor based on lead titanate ($PbTiO_3$) nanoplates [40]. The nanoplates, named P25–$PbTiO_3$ (Fig. 3a), were derived from lead (Pb) precursors and commercial P25 TiO_2 powders via hydrothermal route. Compared to $PbTiO_3$ synthesized from mixtures of pure anatase and rutile powders, P25–$PbTiO_3$ nanoplates showed enhanced sensitivity ($R_g/R_a = 80.4$ at 5 ppm NH_3), and improved sensor response/recovery speed (Fig. 3b), with little response variation in humid ambient (20–80% RH) (Fig. 3c). Ideally, as confirmed by FTIR spectra in (Fig. 3d), humidity (H_2O) can interact with pre-adsorbed O^- forming pronounced OH^- on $PbTiO_3$ along with a release of electrons and a decrease in resistance. Diffuse reflectance infrared Fourier transform (DRIFT) analysis indicated that the intensities of OH peaks remained more or less the same, confirming that the formation of OH^- groups completed at a relatively low humidity, resulting in a negligible variation of response with further increase in humidity.

Several techniques to tailor the functional characteristics of perovskite oxides such as strain induction [9] and doping [20] have been introduced. Particularly, doping or substitution on the A-site of ABO_3 perovskites with aliovalent ions forms ionic and electronic defects, along with charge compensation. Doped perovskites exhibit higher oxygen vacancies [25], enhanced electrical conductivity [41], low-temperature sensing [42], induced catalytic property

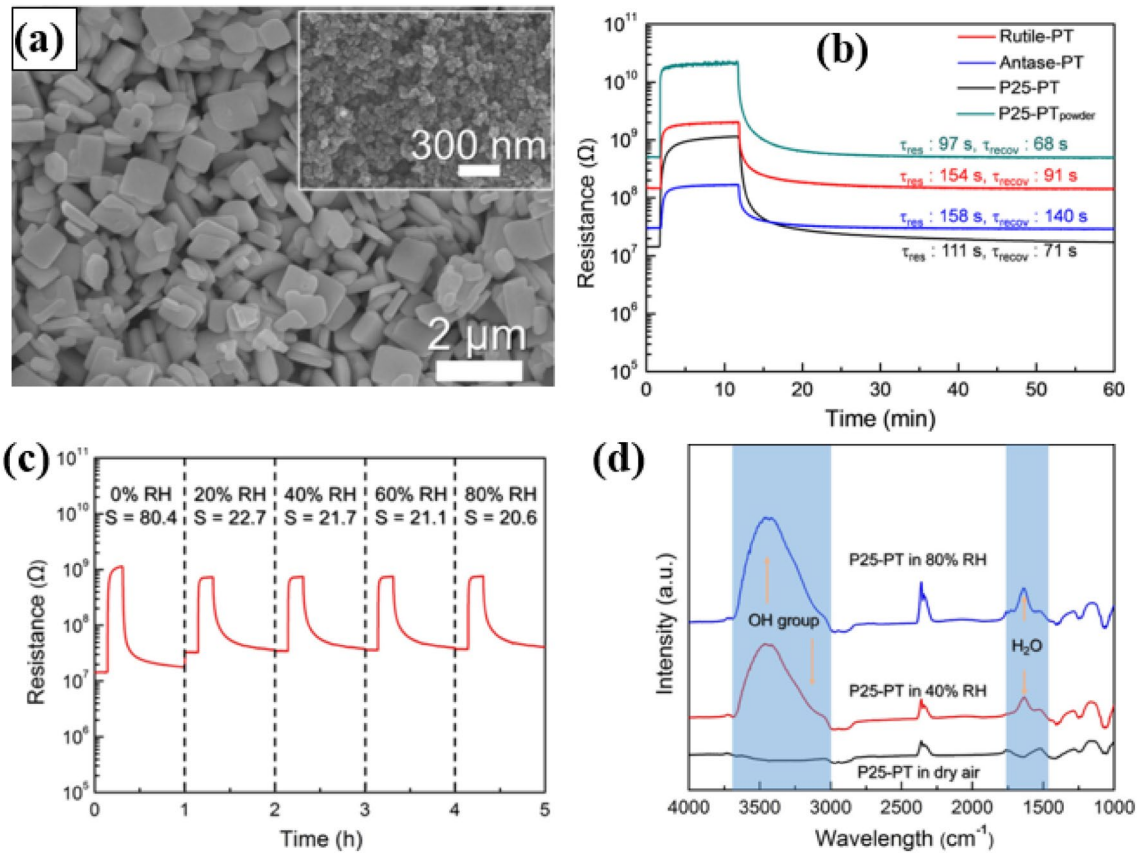

Fig. 3 **a** SEM images of P25-$PbTiO_3$ NPs. The inset is the SEM image of the starting P25 TiO_2 powders. **b** Response–recovery curves of sensors using rutile-PT, anatase-PT, P25-PT, and P25-PT powders to 5 ppm C_2H_5OH at 300 °C, **c** response–recovery curves of the P25-PT sensor to 5 ppm of ethanol in air at 300 °C and different humidity levels. **d** DRIFT spectra of P25-PT in different humidity conditions (dry air, 40 and 80% RH) at 300 °C (Reprinted with permission from Ref. [40]. Copyright (2019) American Chemical Society)

[43], and smaller crystal sizes [20], making them highly suitable for gas-sensing applications. For this reason, many doped ABO_3 perovskites have attracted considerable attention for gas-sensing applications [20, 44–46]. Particularly, perovskite oxides of the form $La_{1-x}M_xFeO_3$ (M = Ba, Sr, Ca, Mg) show good sensing performance and low resistivity compared to basic $LaFeO_3$ [20, 44, 47, 48]. Sun et al. reduced the resistivity of $LaFeO_3$ by doping with barium (Ba), and achieved enhanced ethanol-sensing performance [20]. Likewise, Fan et al. partially substituted La with various amounts (x) of strontium (Sr) to achieve $La_{1-x}Sr_xFeO_3$, which exhibited low resistivity, particularly when $x \leq 0.1$ [45]. Replacement of La^{3+} with Sr^{2+} created Fe^{4+} to maintain the charge neutrality, along with creation of oxygen vacancies. However, for large amount of dopant (Sr), the resistivity of $La_{1-x}Sr_xFeO_3$ increased, as excessive oxygen vacancies were formed along with combination of holes with electrons. Importantly, all these elements, i.e., Ba, Sr, and Ca, belong to the same group, and are very close in the periodic table. In this case, one would expect similar physical properties if they were to be used as dopants for $LaFeO_3$. Recently, Palmar et al. investigated calcium substituted lanthanum ferrite ($La_{0.8}Ca_{0.2}FeO_{2.95}$, henceforth LaCaFeO) nanoparticles for SO_2 sensing [42]. In their study, as the doping level and temperature increased, there was a substantial resistance variation. Normally, substitution of smaller cation Ca^{2+} in the La^{3+} site is likely to reduce the Fe–O-bond length, and introduce a substitutional disorder and oxygen vacancies. Perhaps, it is for this reason that LaCaFeO exhibited higher lattice oxygen vacancies and enhanced p-type semiconducting properties compared to the parent $LaFeO_3$ (LaFeO), influencing its sensitivity, speed, low-temperature sensing, and good recyclability toward SO_2. Ideally, the abundant non-coordinated atoms (dangling bonds) in LaCaFeO are prerequisites for electronically favored reaction sites, an important factor for enhanced SO_2 chemisorption and charge transfer [49]. In principle, Fe readily existed in oxidation states such as Fe^{2+}, Fe^{3+}, and Fe^{4+}, supporting the argument that partial substitution of Fe in $LaFeO_3$ generates active iron species. Natile et al.

found that $LaFe_{1-x}Ga_xO_3$ can be tuned into porous microstructure in parallel with larger crystal sizes as the amount of Ga increases. More importantly, three oxidation states of Fe were unambiguously identified upon insertion of various amounts of Ga ($x=0$–1). Especially, abundance of coordinately unsaturated Lewis acidic sites, i.e., Fe^{4+} (for $x=0.4$), enabled the interaction of numerous oxygen molecules and led to creation of reaction sites for NO_2 adsorption. On the other hand, intermediate species of NO_2 adsorption can play a major role in enhancing the sensitivity upon interaction with surface Fe^{3+} and Fe^{2+} species. It can be concluded here that the fundamental principle for enhanced gas sensing is the creation of numerous oxygen vacancies, which in turn can be consumed by oxygen molecules.

The effect of oxygen vacancies on conductivity in ambient oxygen has been studied by Bektas et al. [50], who prepared $BaFe_{1-x}Ta_xO_{3-\delta}$ by direct mixing of $BaCO_3$, Fe_2O_3, and Ta_2O_5, and carefully controlled the amount of Ta in the range $0.2 \le x \le 0.7$. They then determined the electrical conductivity of the sintered $BaFe_{1-x}Ta_xO_{3-\delta}$ samples in ambient of 1–100% oxygen concentrations and temperature range of 400–900 °C. It was evident that $BaFe_{1-x}Ta_xO_{3-\delta}$ can act as temperature-independent oxygen sensor suitable for applications such as oxygen concentration measurements in automotive exhausts. In fact, its performance is incomparable to oxygen sensing performances of temperature-dependent $SrTiO_3$ and of the SO_2-prone $SrTi_{0.65}Fe_{0.35}O_{3-\delta}$ reported elsewhere [51, 52]. Unlike the classical semiconducting metal oxides, the charge carrier density in $BaFe_{1-x}Ta_xO_{3-\delta}$ is dependent on bulk defect chemistry. Note that the electron (hole) concentration varies linearly with oxygen partial pressure and the electrical conductivity. At higher amount of electron donating Ta (as x reaches 0.5), oxygen deficiency and the electrical conductivity decreased along with switching from *p*-type to *n*-type conductivity.

3 Composites of ABO_3 perovskites and binary metal oxides

Composites comprising dissimilar semiconducting metal oxides exhibit intriguing hallmarks such as heterojunctions and/or close proximity effects that enhance the gas-sensing performance [53–57]. In heterojunctions (*n–n* or *p–n* interfaces), Fermi energy levels across the interfaces of dissimilar oxides in contact would equilibrate along with band bending, causing transfer of charge carriers and creation of charge-depleted regions. Strain-induced defects are also likely to occur due to lattice mismatch, which eventually act as trapping centers for electrons and holes, causing depletion of charge carriers near the interfaces. Inspired by adsorption capability of CaO toward CO_2, Joshi et al. [58] synthesized and utilized *n–n* heterostructures based on CaO–$BaTiO_3$ for CO_2 sensing. Particularly, CaO exhibits higher sorption capacity and fast reaction rate with CO_2, but is prone to aggregation upon sintering [59], and exhibits essentially poor reversibility. Incorporation of CaO into sintering-resistant $BaTiO_3$ not only improves its CO_2 sensing performance, but also eliminates the tendency to aggregate. The precursors materials were mixed, as shown in Fig. 4a, followed by heat treatment to obtained isolated *n–n* crystals (Fig. 4b, c). As shown in Fig. 4d (i), when CaO–$BaTiO_3$ was exposed to CO_2 at room temperature, only physisorption of CO_2 occurred. However, CaO–$BaTiO_3$ reacted with CO_2 to form $CaCO_3$ and $BaCO_3$ as the temperature increased (Fig. 4d(iii)) because CaO and/BaO exhibit high affinity to CO_2. No carbonate bands appeared in the absence of CO_2. Unlike pristine $BaTiO_3$ and CaO that remained almost insensitive even to 1000 ppm CO_2, CaO–$BaTiO_3$ nanocomposite exhibited enhanced response ($\Delta R/R_a$ of 65%) at 160 °C, with superior selectivity against various gases (Fig. 4e). Enhanced response was due to work function difference between CaO (1.69 eV) and $BaTiO_3$ (4 eV), cumulative depletion layer at interfaces following electron–hole recombination in respective $BaTiO_3$ and CaO, as well as adsorption of oxygen molecules on CaO and $BaTiO_3$. Accordingly, adsorption and desorption of CO_2 modulated the resistance of CaO–$BaTiO_3$.

In another investigation, Zhang et al. prepared heterojunctions composed of *p*-type $LaFeO_3$ and *n*-type α-Fe_2O_3 via a facile one-step solvothermal method in accordance with an illustration in Fig. 5a [60]. Using this technique, $LaFeO_3$ was uniformly incorporated into Fe_2O_3, forming *p–n* heterojunctions throughout the porous $LaFeO_3$/α-Fe_2O_3 nano-octahedrons. Note that both α–Fe_2O_3 and $LaFeO_3$ are semiconducting oxides with narrow bandgaps of 2.1 and 2.3 eV, respectively [61], and intriguing gas-sensing properties. Decoration of optimal amount of $LaFeO_3$ onto α-Fe_2O_3 resulted in a threefold enhanced response (Fig. 5b), enhanced selectivity against interfering gases (Fig. 5c), fast response/recovery speed, and sensor stability compared to that of pristine α-Fe_2O_3. Apart from the adsorption/desorption reactions of the air and acetone onto $LaFeO_3$/α-Fe_2O_3 nano-octahedrons, higher response can be attributed to formation of the *p–n* heterostructure. Due to higher Fermi level of α-Fe_2O_3 compared to that of $LaFeO_3$, transfer of charge carriers, i.e., electrons from α-Fe_2O_3 to $LaFeO_3$ and holes from $LaFeO_3$ to α-Fe_2O_3, can occur at the interfaces to equilibrate the Fermi energy levels, resulting in a *p–n* junction. In this way, the band banding and charge depletion layer at the *p–n* junction increased the base resistance of $LaFeO_3$/α-Fe_2O_3 composite (264 MΩ) in the air compared to that of unmodified α-Fe_2O_3 (23 Ω), thus increasing the response of the $LaFeO_3$/α-Fe_2O_3 composite.

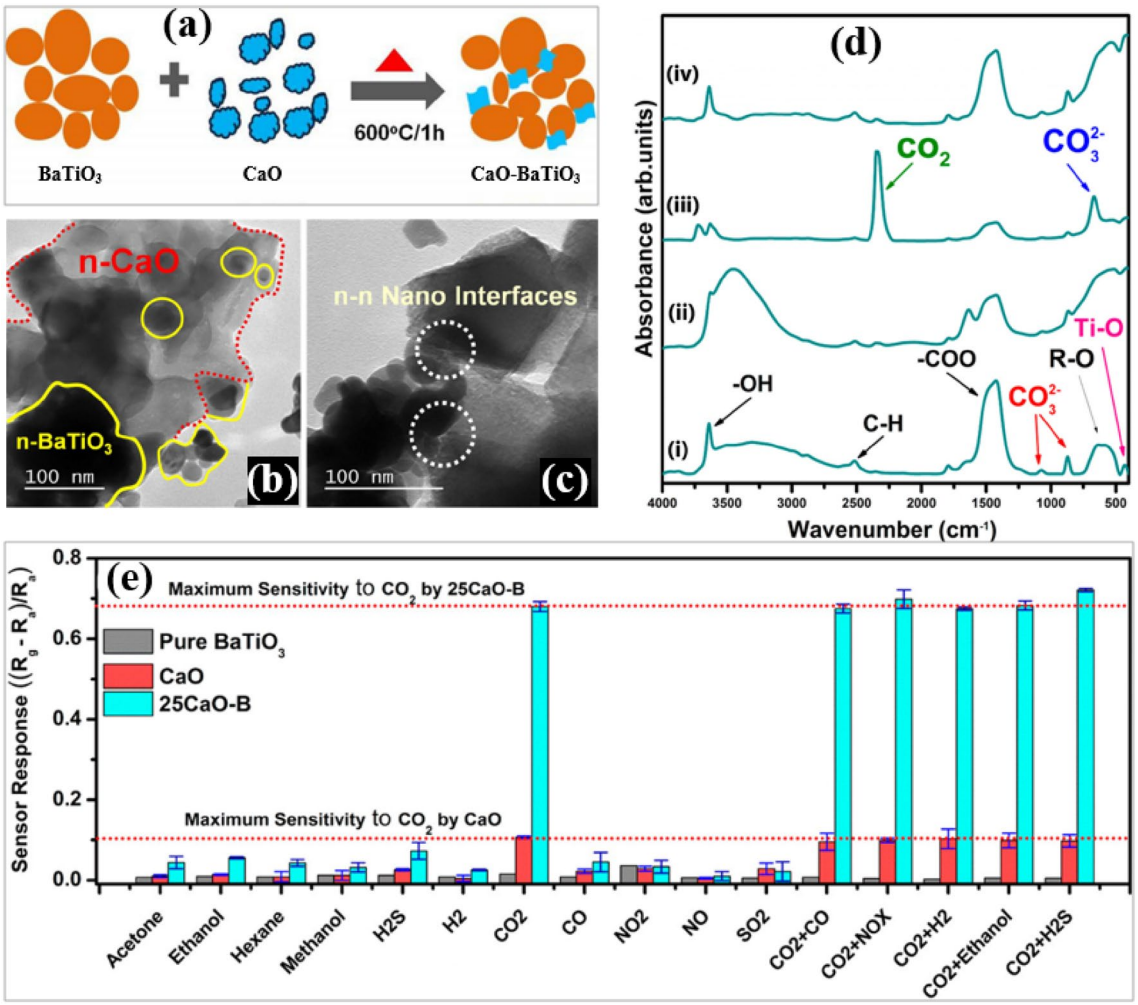

Fig. 4 **a** Synthesis route of CaO-$BaTiO_3$ based *n–n* heterostructures, **b**, **c** *n–n* interfaces of $BaTiO_3$ spheroids and CaO sheets, **d** diffuse reflectance infrared Fourier transform spectra of 25CaO-B at room temperature, in absence of CO_2 gas at 160 °C, in the presence of CO_2 gas at 160 °C, and at room temperature in the absence of CO_2 gas, shown as i–iv, respectively. **e** Dominant selectivity toward 1000 ppm of CO_2 gas concentration balanced with dry synthetic air at 160 °C. The interfering gases are acetone (500 ppm), ethanol (500 ppm), hexane (1000 ppm), methanol (500 ppm), H_2S (100 ppm), H_2 (50 ppm), CO (50 ppm), NO_2 (1000 ppm), NO (100 ppm), and SO_2 (50 ppm) (Reprinted with permission from Ref. [58]. Copyright (2018) American Chemical Society)

4 Catalyst loaded ABO_3 perovskites

Apart from doping of A and/or B site in ABO_3 perovskites or combination with metal oxides, catalysts loading on these perovskite oxides can provide specific adsorption sites for oxygen adsorption and catalytic centers for oxidation of analyte gases to improve sensors response, speed, selectivity, and operating temperature. Thus far, various perovskite oxides have been loaded with various catalysts such as silver (Ag) [62–64], palladium (Pd) [65, 66], and Au [67] for gas-sensing applications. These catalysts can physically or chemically interact with the surface of perovskite oxides depending on synthesis conditions and nature of catalysts. Typically, the method of catalyst loading on host materials and the interaction thereof can influence how the material responds to various gases. For instance, Wei et al. [62] loaded Ag in $LaFeO_3$ and observed that most Ag remained as isolated catalysts on the surface of $LaFeO_3$, whereas some of Ag ions replaced La^{3+}, forming defects and holes therein. The introduced defects provided more holes, leading to high charge carrier concentration and enhancement of formaldehyde sensing. Joshi et al. [64] prepared Ag@CuO—decorated $BaTiO_3$ spheroids by wet impregnation and hydrothermal techniques, and investigated their sensing affinity to CO_2. Here, intermittent *p–n* heterojunctions were formed upon co-precipitation of CuO microleaves with $BaTiO_3$ spheroids. Then, different amounts of metallic Ag (0.5–1.5 wt %) were loaded on *p*-CuO/*n*-$BaTiO_3$ composite via impregnation into ethanol containing $AgNO_3$. Formation of *p–n* heterojunction resulted in significant improvement

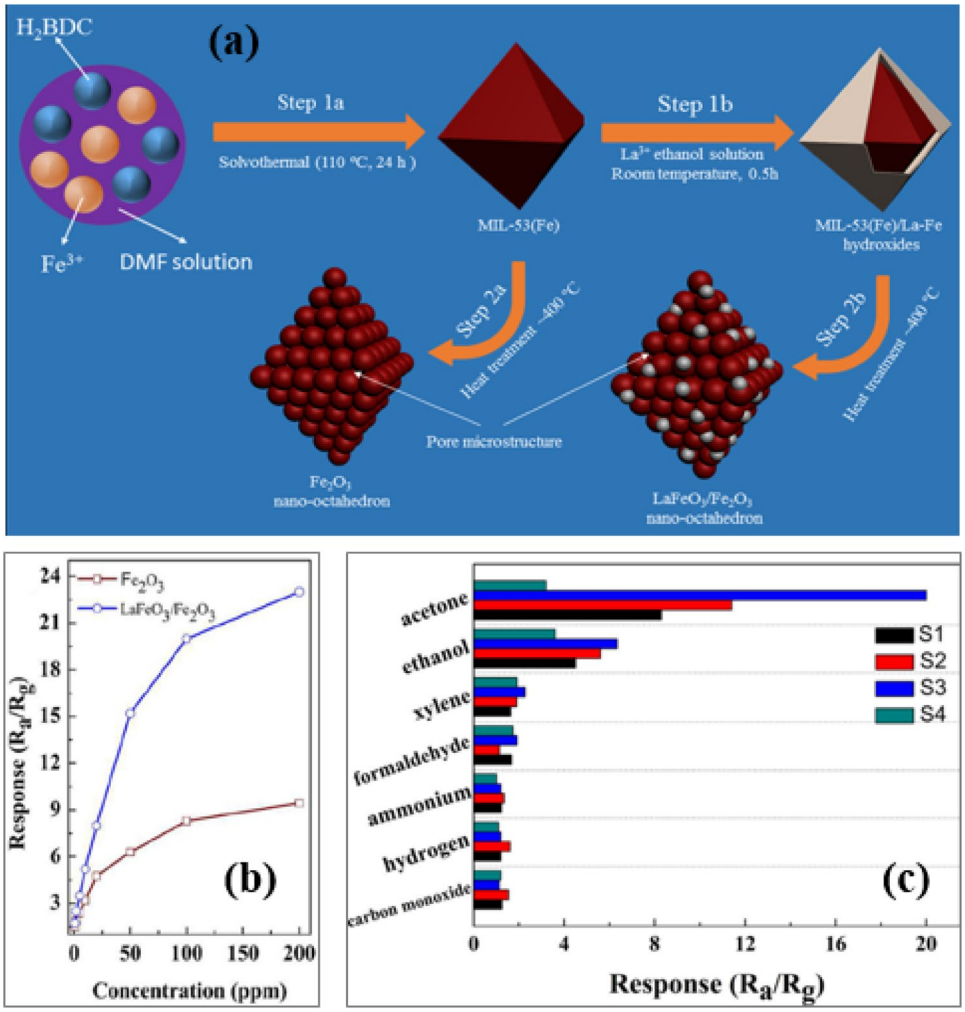

Fig. 5 **a** Schematic illustrating the synthesis of porous α-Fe_2O_3 nano-octahedrons and $LaFeO_3$/α-Fe_2O_3 Composites, **b** responses of the pure α-Fe_2O_3 and $LaFeO_3$/α-Fe_2O_3 composites to different concentrations of acetone, and **c** selectivity of α-Fe_2O_3 and various $LaFeO_3$/α-Fe_2O_3 composites to 100 ppm of various gases. S1–S4 samples denoted composites containing different amounts of $LaFeO_3$ (Reprinted with permission from Ref. [60]. Copyright (2018) American Chemical Society)

of the sensor response, which increased with the amount of CuO, until equimolar CuO/$BaTiO_3$ was obtained. At this condition, a very low limit of detection (~51 ppm) was obtained. After decoration of 1% Ag on equimolar CuO/$BaTiO_3$, the results were highly repeatable and accurate, with a response ($\Delta R/R_a$) of 58.64%, and fast recovery toward 1000 ppm at 120 °C, because Ag can readily catalyze the adsorption of CO_2. In the presence of the catalyst, the limit of detection decreased to ≈41 ppm. Moreover, $CuCO_3$ and $BaCO_3$ were formed after adsorption of CO_2 on CuO/$BaTiO_3$, which possibly enhanced the response and selectivity toward CO_2. This was in agreement with the work of Joshi and coauthors [58].

Cao et al. investigated the influence of Au and Cl loading on $LaFeO_3$ [67]. The loading of Au and Cl was achieved by addition of different weight proportions ($x = 0$, 0.5, and 1 wt %) of $HAuCl_4$ during the sol–gel synthesis. Their analyses showed that heat treatment of $LaFeO_3$ precursors and $HAuCl_4$ in organic solvents evolved CO_2, which was capable of reacting with superficial La–O in the as-formed $LaFeO_3$, resulting in La-carbonate. This occurred in concurrence with formation of Fe–Cl and La–Cl bonds after chemisorption of Cl on Fe sites in the FeO_6 octahedra (Fig. 6a, steps 1–2), and replacement of C=O bond in monodentate La-carbonate with the C–Cl bond. On the other hand, Au existed as physically adsorbed particles on $LaFeO_3$ crystals (step 3). Co-existence of Au, Cl, and Fe ions sites in the $LaFeO_3$ facilitated massive adsorption of oxygen and ethanol (steps 4–5), with the highest adsorption observed at $x = 1$ wt %. Co-modification of $LaFeO_3$ with Au and Cl resulted in an increase of charge transfer (90.7%) from ethanol to the adsorbed oxygen on the Fe–O-terminated $LaFeO_3$ surface. In this way, the Au- and Cl-modified $LaFeO_3$ exhibited the highest reported response ($R_g/R_a = 220.7$) and selectivity toward 100 ppm ethanol (Fig. 6b, c).

5 ABO_3 perovskites as catalysts

Perovskite oxides are of interest as alternatives for noble metal catalysts in a broad range of applications [68–73]. Adoption of perovskite oxides as catalyst aims at designing

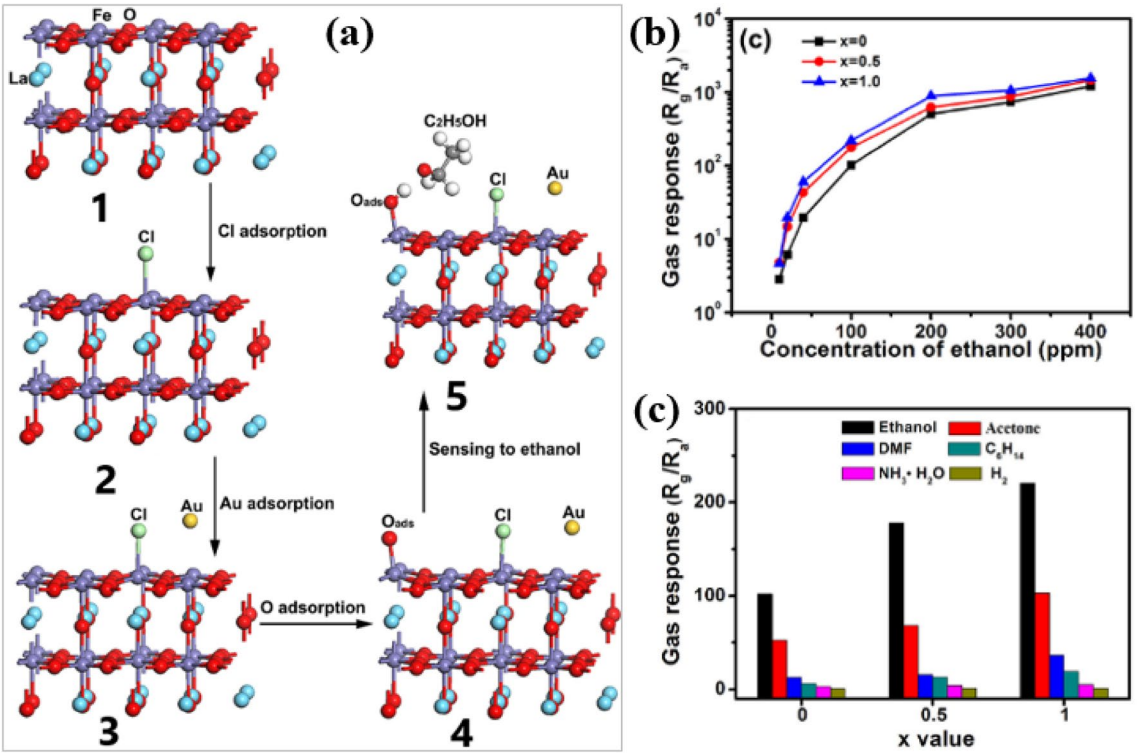

Fig. 6 **a** Stable configuration of FeO-terminated $LaFeO_3$ (001) surface, with Cl, Au, and O adsorption as well as final ethanol adsorption indicated as 1–5, respectively. Cyan, purple, red, green, yellow, gray, and white balls represent La, Fe, O, Cl, Au, C, and H atoms, respectively. **b** Gas responses of Au- and Cl-modified $LaFeO_3$ NPs to 10–400 ppm ethanol, and **c** 100 ppm of different gases at 120 °C (Reprinted with permission from Ref. [67]. Copyright (2019) American Chemical Society)

of thermochemical-stable, cost-effective, and highly active catalysts to overcome prohibitive cost, poor thermal stability, poisoning effects, and scarcity of noble metal catalysts. In this perspective, application of perovskite oxides as catalysts in gas-sensing applications cannot be an exception, particularly in those involving high-temperature operation and hash chemical environments. Despite few attempts to elucidate catalytic effects of ABO_3 perovskites in gas-sensing applications [74–76], reports in this area are still scarce.

Lin and coauthors have investigated the effect of $La_{0.8}Sr_{0.2}FeO_3$ (LSFO) particles on β-Ga_2O_3 nanorods ($\approx$ 100–300 nm thick) via sputtering technique and thermal annealing [75]. In their approach, they synthesized and employed LSFO–decorated β-Ga_2O_3 nanorods for detection of carbon monoxide (CO). For comparison purposes, they also prepared and decorated β-Ga_2O_3 nanorods with ultrasmall Pt nanoparticles (30 wt %), a higher loading amount compared to $\approx$ 1.22 wt % of LSFO. Similar to distinctive chemical sensitization and spillover effects of Pt catalysts [77], LSFO particles with suitable composition exhibited spillover effect on Ga_2O_3 nanorods owing to the presence of oxygen vacancies, which increased their oxygen adsorption capability (Fig. 7a). Unlike bare *n*-type β-Ga_2O_3, abundant oxygen can be adsorbed on LSFO particles. Moreover, further charge-depleted regions were created at interfaces of *p*-type LCFO and *n*-type β-Ga_2O_3 because of differences in Fermi levels. Since CO is an electron donor, when it was adsorbed on the surface of LSFO–decorated β-Ga_2O_3, the depletion layer became thinner along with an increase of the overall electrical conductivity (Fig. 7b). Since the reaction of O^- and CO was small on LSFO, there existed a concentration gradient between abundant unconsumed O^- species on the surface of LSFO and those adsorbed on β-Ga_2O_3 nanorods. Moreover, as indicated in Fig. 7c, O^- species were attracted from LSFO particles toward the interfaces of LSFO and β-Ga_2O_3 nanorods, which eventually spilled over onto the surface of β-Ga_2O_3 nanorods. Surprisingly, LSFO decorated β-Ga_2O_3 nanorods indicated a similar sensitivity (R_O/R_{CO}, where R_O is the resistance in N_2, and R_{CO} is the resistance in CO/N_2 mixture) to that of Pt-decorated β-Ga_2O_3 nanorods, despite a small amount of LSFO particles (5 and 10 nm thick) used (Fig. 7d). This result implies that LSFO can equally replace Pt catalysts. Although fast response was observed for the LSFO decorated β-Ga_2O_3 nanorods compared to Pt-decorated β-Ga_2O_3 ones (Fig. 7e), this response was not faster than that observed for pristine β-Ga_2O_3 nanorods.

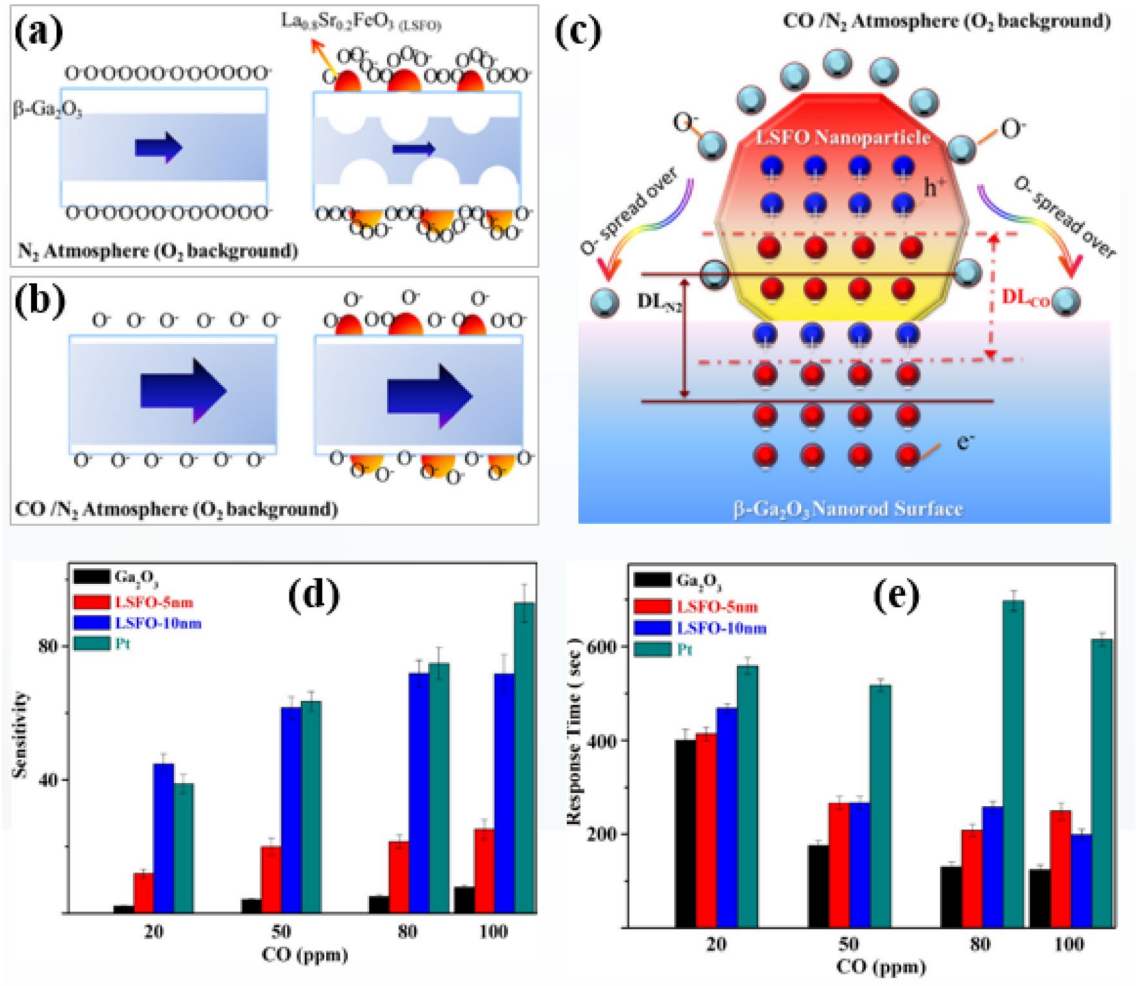

Fig. 7 Gas-sensing enhancement mechanism of **a** β-Ga_2O_3 and LSFO decorated β-Ga_2O_3 nanorods in N_2 atmosphere, **b** β-Ga_2O_3 and LSFO decorated β-Ga_2O_3 nanorods in CO/N_2 atmosphere. **c** Spillover-like effect model in LSFO nanoparticle decorated β-Ga_2O_3 nanorods surface in CO/N_2 atmosphere. DL stands for carrier depletion layer. **d** Sensitivity [R_O/R_{CO}, where R_O is the resistance in N_2, and R_{CO} is the resistance in CO/N_2 mixture] of β-Ga_2O_3, β-Ga_2O_3/LSFO, and β-Ga_2O_3/Pt composite nanorods tested at 500 °C, and **e** response time of β-Ga_2O_3, β-Ga_2O_3/LSFO, and β-Ga_2O_3/Pt composite nanorods tested at 500 °C (Reprinted with permission from Ref. [75]. Copyright (2016) American Chemical Society)

Another interesting work is that of Kang et al., in which the catalytic role of quasispherical $La_{0.75}Sr_{0.25}Cr_{0.5}Mn_{0.5}O_{3-\delta}$ (LSCM) particles (215.7 nm-diameter) in SnO_2 fiber-in-tube (FITs) was investigated for formaldehyde (HCHO) sensing [76]. A versatile electrospinning technique was used to electrospin a solution containing LCSM particles and SnO_2 precursor, as demonstrated in Fig. 8a. It was observed that LSCM inhibited the grain growth and hindered Oswald ripening mechanisms, enabling the formation of LSCM-loaded SnO_2 FITs architectures (Fig. 8b). Apart from easy penetration of air and HCHO in the tubes as well as surface pores, LSCM can enhance HCHO sensing due to formation of heterojunctions with SnO_2, and the presence of oxygen vacancies (Fig. 8c), similar to LSFO particles demonstrated by Lin et al. [75]. The heterojunction effect is attributed to work function differences between LSCM (6.8 eV) and SnO_2 (4.55 eV) that can cause band bending and depletion of charge carriers at interfaces along with an increase in the base resistance. Abundant oxygen vacancies can be created upon partial substitution of La with Sr, as well as possible reduction of Mn^{4+} to Mn^{3+} following charge migration during the formation of heterojunctions. Ideally, O^- can weakly adsorb into oxygen vacancies, but can exist in abundance on the surface of LSCM particles. These oxygen species can easily spread over the surface of SnO_2 by spillover effect. In fact, the ratio of chemisorbed O^- species to lattice O^{2-} in LSCM was larger than in bare SnO_2 (0.9 vs 1.48) when determined at 400 °C. Because of these events, the response of LSCM-loaded SnO_2 FITs was higher than that of SnO_2 nanotubes (NTs), SnO_2 NFs, and that of the reference sensor,

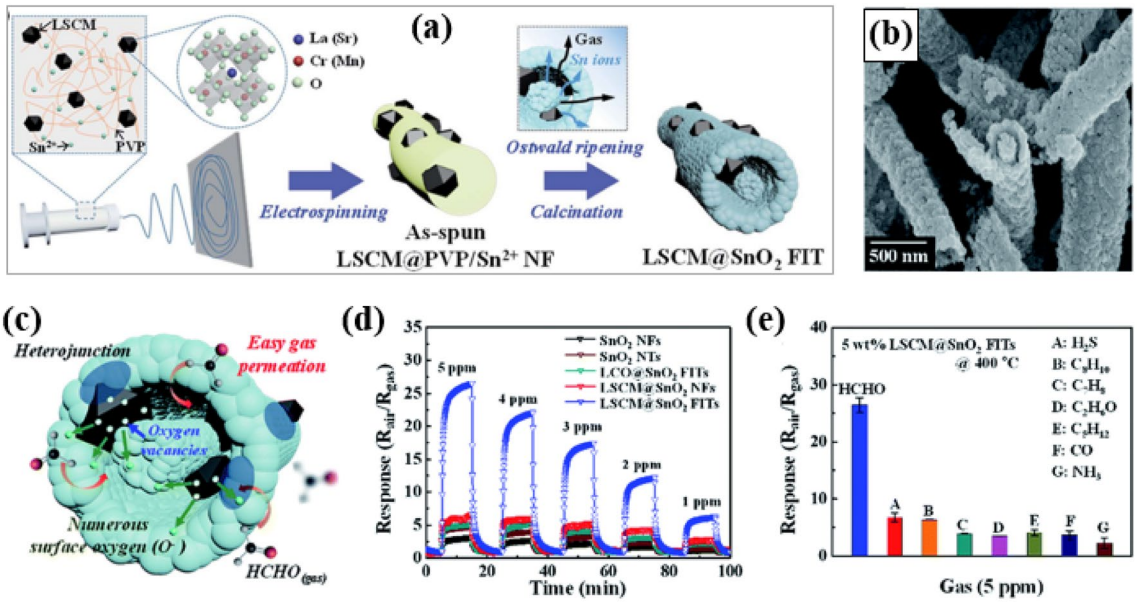

Fig. 8 **a** Schematic indicating the synthesis procedure for LSCM@SnO_2 FITs, **b** morphology of LSCM@SnO_2 FITs, **c** illustration of HCHO sensing mechanism of LSCM@SnO_2 FITs, **d** response/recovery profiles for different sensors toward 1–5 ppm HCHO at 400 °C, and **e** selectivity property of LCSM@SnO_2 FITs toward various gases at 400 °C (Reproduced from Ref. [76] with permission from The Royal Society of Chemistry)

i.e., LCO loaded SnO_2 FITs (Fig. 8d). More importantly, the sensitivity of LSCM–loaded SnO_2 FITs toward HCHO was significantly higher than toward interfering gases (Fig. 8e).

6 Porosity control in ABO_3 perovskites

Fast diffusion of oxygen in perovskite oxides depends on availability of oxygen vacancies, usually tuned by optimizing material composition. In addition, porosity control is essential. It is well known that porous nanostructures possess higher concentration of active sites than their dense analogues [78, 79]. In general, thick semiconducting metal oxides experience prominent gas diffusion and reaction effects owing to longer diffusion depths, leading to gas-inaccessible reaction sites and low sensitivity. The gas concentration decays with the diffusion length because of an instantaneous reaction between the incoming analytes and the abundant pre-absorbed oxygen species [79]. This implies that the rate of consumption due to gas reaction approaches the rate of accumulation of analytes. Under a combination of optimal diffusion depth with pore apertures (mesopores and/or macropores), such decay of concentration can be eliminated. To achieve this, one needs to control the porosity of sensing materials. Currently, several techniques to introduce porosity in metal oxides have been suggested: such approaches include apoferritin templating [80, 81], chitosan templating [82], soft templating [83], and hard templating [84–90], among many others. Unfortunately, ABO_3 perovskites mainly used in gas-sensing applications are those based on solid-state reactions of precursor powders [44, 50] or sputtered films [28, 91]. In addition, with few exceptions such as the work demonstrated by Ma et al., [92] and others [29, 62, 93, 94], even electrospun perovskite oxides still exhibit limited porosity. The most promising, however, are the works of Xiao et al. [35] and Wang et al. [95] that employ a simple Ostwald ripening to synthesize porous perovskite oxides. However, despite the fact that Ostwald ripening is a template-free technique, it is difficult to achieve controlled grain/pore size and morphological tuning of ABO_3 perovskite materials. Recently, hard templating approaches for porosity control in perovskite oxides were elucidated [96–100]. Typically, hard templating involves introduction of rigid templates such as solid or mesoporous silica, carbon, and polystyrene (PS) beads, whose elimination by calcination or dissolution in chemicals (acids or alkali etchants) creates various porous and hollow structures, ranging from simple to intricate ones. Dai and coworkers employed sacrificial PS beads to template porosity in a $LaFeO_3$ film. As illustrated in Fig. 9a, a self-organized monolayer of monodispersed PS beads (500 nm-diameter) was floated on a mixed precursor solution containing La^{3+} and Fe^{3+}, followed by a pickup of the precursor coated beads using a substrate printed with sensing and heating electrodes. After drying and heat treatment, honeycomb-like porous thin film was formed. Following a high degree of ordering of PS beads on the silicon substrate (Fig. 9b), a periodic porous film of octahedral $LaFeO_3$ was

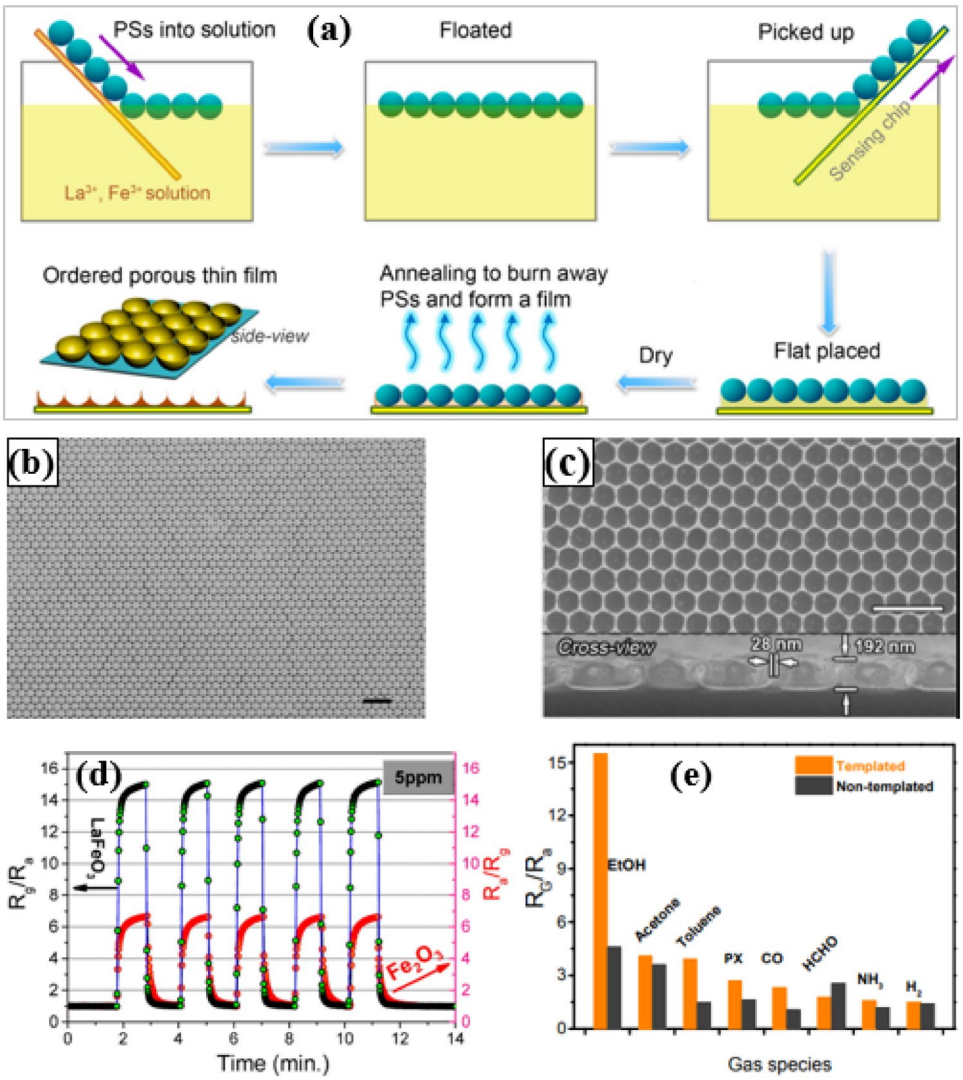

Fig. 9 **a** Schematic for fabrication of $LaFeO_3$-ordered porous thin films. Morphological and microstructural characterizations of **b** a PS microsphere (500 nm in diameter) monolayer and **c** $LaFeO_3$-ordered porous film. Sensing response of **d** $LaFeO_3$ and Fe_2O_3 porous thin film sensors at 450 °C for five gas-on/off cycles upon exposure to 5 ppm ethanol, and **e** the response of template-directed $LaFeO_3$ and non-template $LaFeO_3$ films toward 5 ppm of different gases at 450 °C (PX: *p*-xylene) (Reprinted with permission from Ref. [96] Copyright (2014) American Chemical Society)

obtained after thermal treatment (Fig. 9c). The thickness of the film was determined to be 192 nm, whereas the thickness of the pore wall was 28 nm. Ideally, even the sizes of pores previously occupied by PS beads are expected to be 40–60% smaller due to shrinkage as PS beads decompose in the temperature range of 325–390 °C [87]. Because of numerous oxygen vacancies in $LaFeO_3$, the ratio of adsorbed to lattice oxygen species (O^-/O^{2-}) was even higher than that of Fe_2O_3 prepared by a similar technique. The porous morphology and enhanced surface oxygen resulted in a stable high response (Fig. 9d), fast response speed (≈4 s), and low limit of detection (50 ppb) of porous $LaFeO_3$ films toward ethanol compared to that of porous Fe_2O_3 film. Importantly, the templated $LaFeO_3$ exhibited a high selectivity to ethanol compared to that of a non-templated $LaFeO_3$ film (Fig. 9e), confirming the effect of pores in gas sensing.

Considering enhanced sensing performance of heterogeneous perovskite oxides compared to their single-phase analogues, further enhancement in performance can be achieved if adsorption/desorption kinetics of oxygen and target gases were enhanced. Chen et al. [97] prepared Ag/Zn-$LaFeO_3$ nanocomposite via nanocasting technique, with KIT-6 (i.e., Korea Institute of Technology-6) as a template. KIT-6 is a three-dimensional (3D) silica material with high surface area and ordered mesostructure. Xu et al. have reported the surface area of KIT-6 as high as 635 $m^2\ g^{-1}$ and mesopore sizes in the range of 8–10 nm [101]. Chen and coworkers prepared KIT-6 in accordance with the procedure described in Fig. 10a. Precursors of Ag/Zn-$LaFeO_3$ were infiltrated into KIT-6 followed by heat treatment and silica etching in NaOH to achieve crystalline porous Ag/Zn-$LaFeO_3$ nanocomposites containing various amounts of Zn. In a perfect $LaFeO_3$ crystal, all sites would consist of La^{3+}, Fe^{3+}, and O^{2-} ions. However, with 2 at % Zn doping (with respect to La or Fe), two states of Fe, i.e., Fe^{3+} and Fe^{4+} coexisted. Typically, Fe^{4+} can readily interact with oxygen molecules, creating numerous reaction sites for target gases. In addition, Zn^{2+} would partially substitute La^{3+}, creating defects

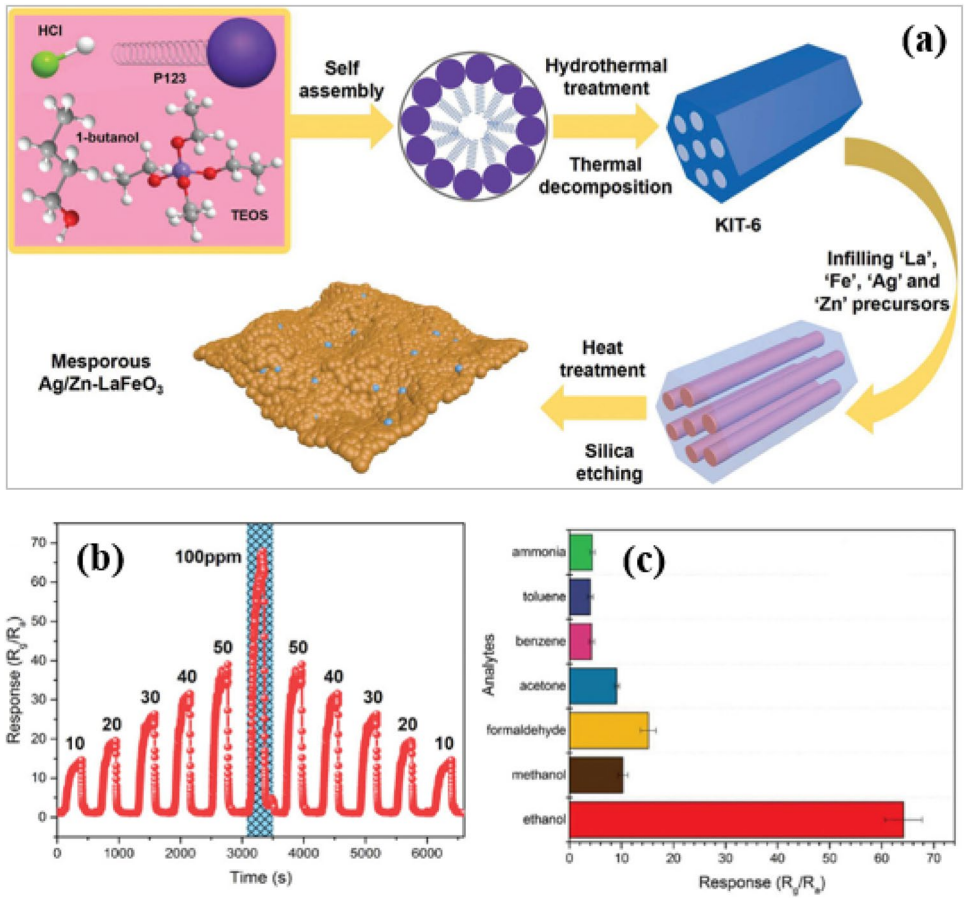

Fig. 10 **a** Schematic for synthesis of KIT-6 templated mesoporous Ag/Zn–$LaFeO_3$ nanocomposites, **b** response and recovery profiles of AZLFO-2 to ethanol in the concentration range of 10–100 ppm at 55 °C, and **c** responses of AZLFO-2 sensors upon exposure to 100 ppm of various volatile organic compounds at 55 °C (Reproduced from Ref. [97] with permission from John Wiley & Sons, Inc.)

on La sites, and charge carriers (holes), whose concentration increases with the amount of Zn dopants. On the other hand, Ag existed as an isolated phase in Ag/Zn-$LaFeO_3$, and possibly played a catalytic role for gas-sensing reactions. This templating approach provided Ag/Zn-$LaFeO_3$ nanocomposites (2 at % Zn, hence forth AZLFO-2) with distinguishable mesopores (3.4 nm in size) and high surface area (118 $m^2\ g^{-1}$). Upon exposure of AZLFO-2 to various concentrations of ethanol at 55 °C, an outstanding response of 64.2 at 100 ppm and a response/recovery speed of 100/20 s were achieved (Fig. 10b). The AZLFO-2 sensor also showed good selectivity toward various gases (Fig. 10c). During exposure, ethanol dissociated into more reactive CH_3CHO that subsequently reacted with adsorbed oxygen, thinning the hole accumulation layer, and leading to high response.

7 Summary and outlook

We have given a brief review of the approaches adopted by most researchers to enhance the sensing performance of ABO_3 perovskites as resistive-type gas-sensing materials. It is noteworthy to mention that perovskite oxides are intrinsically enriched with oxygen vacancies that influence oxygen adsorption. When a tetravalent B site of ABO_3 perovskite is doped with trivalent cation, the resulting oxygen vacancies can dissolve humidity, forming OH^- groups that eventually bind to oxygen in the perovskite lattice. This could potentially affect the sensing performance of perovskite oxides and long-term stability in humid ambient. To further tune physico-chemical properties of perovskite oxides for enhanced gas-sensing performance, one needs to employ various techniques such as (1) heterovalent cation substitution to create anionic and/or cationic vacancies, (2) functionalization with catalysts that display high-effective catalytic activity, and (3) introduction of heterojunctions. Table 1 presents recently reported gas-sensing performance of ABO_3 perovskites. Despite strenuous efforts made thus far, the sensing property such as response to trace (sub-ppm) concentrations and response/recovery speed of ABO_3 perovskites seems far inferior compared to those of binary semiconducting metal oxides (SMOs) reported in several treatises [102, 103]. Moreover, several ABO_3 perovskites can be employed as gas-sensing materials at low temperature, although temperature variation is associated with structural phase transition of some perovskite oxides, indicating that they are unstable at low temperature.

Table 1 Recently reported resistive-type gas sensors based on perovskite oxides and perovskite oxide decorated semiconducting metal oxides

Sensing material	Synthesis technique	Response definition	Sensitivity	Response/recovery times (s)	Target gas	Temp. (°C)	Refs.
Macroporous $LaFeO_3$	PMMA templating	R_g/R_a	96 at 100 ppm	25/23	Methanol	190	[7]
$LaFeO_3$ Nanocubes	Sputtering	$\Delta R/R$	157.89% at 5 ppm	11/15	NO_2	25	[28]
$PrFeO_3$ Hollow NFs	Electrospinning	R_g/R_a	6 at 10 ppm	4/4	Acetone	180	[92]
Porous $LaFeO_3$ microspheres	Hydrothermal	R_g/R_a	29 at 100 ppm	9/17	Acetone	260	[35]
$PbTiO_3$ nanoplates	Hydrothermal	R_g/R_a	80.4 at 5 ppm	97/68	Ethanol	300	[40]
$La_{0.8}Ca_{0.2}FeO_{2.95}$ nanoparticles	Soft polymerizable complex	$\Delta R/R_a$	50% at 3 ppm	86/110	SO_2	~275	[42]
$La_{0.95}Mg_{0.05}FeO_3$	PMMA templating	R_g/R_a	146.2 at 100 ppm	17.7/25.4	Methanol	190	[48]
$LaFe_{0.96}Ga_{0.4}O_3$	Citrate gel method	$\Delta R/R$	40 at 200 ppm	Not determined	Ethanol	450	[8]
$LaFeO_3/\alpha$-Fe_2O_3 nanooctahedron	PS templating	R_a/R_g	21 at 100 ppm	1/3	Acetone	230	[60]
CuO-$BaTiO_3$	Hydrothermal and coprecipitation	R_g/R_a	1.24 at 700 ppm	5/18	CO_2	120	[64]
Ag–CuO–$BaTiO_3$	Hydrothermal and coprecipitation	R_g/R_a	1.4 at 700 ppm	3/5	CO_2	120	[64]
Ag-$LaFeO_3$ NPs	Lotus Leaves biotemplating	R_g/R_a	16.76 at 10 ppm	68/36	Xylene	125	[104]
Ag-$LaFeO_3$ nanofibers	Electronspinning	R_g/R_a	4.8 at 5 ppm	2/4	HCHO	230	[62]
Pd:$SmFe_{0.9}Mg_{0.1}O_3$ powders	Sol–gel	R_g/R_a	7.16 at 0.5 ppm	32/8	Acetone	220	[65]
Au and Cl Comodified $LaFeO_3$ Nanoparticles	Sol–gel	R_g/R_a	220.7 at 100 ppm	35/-	Ethanol	120	[67]
$LaMnO_3$@ZnO nanoflowers	Hydrothermal	R_a/R_g	~6.2 at 50 ppm	37/32	Ethanol	300	[74]
$La_{0.8}Sr_{0.2}FeO_3$ decorated β-Ga_2O_3 nanorods	Hydrothermal and sputtering	(R_o/R_{CO})-1	70 at 100 ppm	≈200/>400	CO	500	[75]
$La_{0.75}Sr_{0.25}Cr_{0.5}Mn_{0.5}O_3$ sensitized SnO_2 Fiber-in-tube	Electrospinning	R_a/R_g	26.5 at 5 ppm	<32/254.4	HCHO	400	[76]
$LaMnO_3$-SnO_2 nanofibers	electrospinning	R_a/R_g	20 at 100 ppm	6/34	Ethanol	260	[93]
Ag/Zn–$LaFeO_3$ nanocomposite	KIT-6 templating	R_g/R_a	64.2 at 100 ppm	100/20	Ethanol	55	[97]
Ca-doped $BiFeO_3$	Sol–gel	R_g/R_a	212 at 500 ppm	90/240	H_2	250	[105]

Despite a significant step for utilization of ABO_3 perovskites as potential alternatives for noble metal catalysts in various applications, their utilization in gas sensing is still at infant stage. In fact, some ABO_3 perovskites are chemically unstable, especially in the presence of gases such as SO_2, limiting their commercialization as catalysts. Other issues relate to small surface area, since their synthesis procedures typically involve high temperature as well as longer heat treatment. Moreover, it is challenging to attain ultrasmall (sub 10 nm-scale) size particles such as those readily achieved for noble metal catalysts like Pt, Pd, Ag, and Au. It is noteworthy to mention that even bulk perovskite oxides exhibit poor porosity for diffusion of analyte gases. In this regard, we have elucidated techniques commonly involved to introduce porosity in perovskite oxides for improving gas sensing. It is anticipated that future investigations will make use of techniques commonly employed in creating pores in binary SMOs such as soft templating, to prepare porous perovskite oxides with various morphologies.

Acknowledgements This work was supported by the Ministry of Trade, Industry and Energy (Korea) under the Industrial Technology Innovation Program (No. 10070075) and the National Research Foundation of Korea (NRF), Grant No. 2014R1A4A1003712 (BRL Program). This work was also supported by Wearable Platform Materials Technology Center (WMC) funded by National Research Foundation of Korea (NRF) Grant of the Korean Government (MSIP) (No. 2016R1A5A1009926).

References

1. M.A. Pena, J.L.G. Fierro, Chemical structures and performance of perovskite oxides. Chem. Rev. **101**(7), 1981–2018 (2001)
2. P. Porta, S. Cimino, S. De Rossi, M. Faticanti, G. Minelli, I. Pettiti, $AFeO_3$ (A = La, Nd, Sm) and $LaFe_{1-x}Mg_xO_3$ perovskites: structural and redox properties. Mater. Chem. Phys. **71**(2), 165–173 (2001)
3. K. Zhang, J. Sunarso, Z. Shao, W. Zhou, C. Sun, S. Wang, S. Liu, Research progress and materials selection guidelines on mixed conducting perovskite-type ceramic membranes for oxygen production. RSC Adv. **1**(9), 1661–1676 (2011)
4. H. Mizoguchi, P.M. Woodward, S.H. Byeon, J.B. Parise, Polymorphism in $NaSbO_3$: structure and bonding in metal oxides. J. Am. Chem. Soc. **126**(10), 3175–3184 (2004)
5. H. Wu, F. Li, Oxygen vacancy-assisted high ionic conductivity in perovskite $LaCoO_{3-\delta}$ ($\delta = 1/3$) thin film: a first-principles-based study. Phys. Lett. A **383**(2-3), 210–214 (2019)
6. M. Cherry, M.S. Islam, C.R.A. Catlow, Oxygen ion migration in perovskite-type oxides. J. Solid State Chem. **118**(1), 125–132 (1995)
7. J. Qin, Z. Cui, X. Yang, S. Zhu, Z. Li, Y. Liang, Synthesis of three-dimensionally ordered macroporous $LaFeO_3$ with enhanced methanol gas sensing properties. Sens. Actuators B **209**, 706–713 (2015)
8. M.M. Natile, A. Ponzoni, I. Concina, A. Glisenti, Chemical tuning versus microstructure features in solid-state gas sensors: $laFe_{1-x}Ga_xO_3$, a case study. Chem. Mater. **26**(4), 1505–1513 (2014)
9. J. Hwang, Z. Feng, N. Charles, X.R. Wang, D. Lee, K.A. Stoerzinger, S. Muy, R.R. Rao, D. Lee, R. Jacobs, *Tuning perovskite oxides by strain: electronic structure, properties, and functions in (electro) catalysis and ferroelectricity* (Mater, Today, 2019)
10. H.J. Kim, U. Kim, T.H. Kim, J. Kim, H.M. Kim, B.-G. Jeon, W.J. Lee, H.S. Mun, K.T. Hong, J. Yu, Physical properties of transparent perovskite oxides (Ba, La) SnO_3 with high electrical mobility at room temperature. Phys. Rev. B **86**(16), 165205 (2012)
11. M.M. Kuklja, Y.A. Mastrikov, B. Jansang, E.A. Kotomin, The intrinsic defects, disordering, and structural stability of $Ba_xSr_{1-x}Co_yFe_{1-y}O_{3-\delta}$ perovskite solid solutions. J. Phys. Chem. C **116**(35), 18605–18611 (2012)
12. S. Švarcová, K. Wiik, J. Tolchard, H.J.M. Bouwmeester, T. Grande, Structural instability of cubic perovskite $BaxSr_{1-x}Co_{1-y}Fe_yO_{3-\delta}$. Solid State Ionics **178**(35-36), 1787–1791 (2008)
13. G. Catalan, J.F. Scott, Physics and applications of bismuth ferrite. Adv. Mater. **21**(24), 2463–2485 (2009)
14. B. Han, K.A. Stoerzinger, V. Tileli, A.D. Gamalski, E.A. Stach, Y. Shao-Horn, Nanoscale structural oscillations in perovskite oxides induced by oxygen evolution. Nat. Mater. **16**(1), 121 (2017)
15. K.D. Kreuer, Proton-conducting oxides. Annu. Rev. Mater. Res. **33**(1), 333–359 (2003)
16. M.A. Gomez, D.L. Fry, M.E. Sweet, Effects on the proton conduction limiting barriers and trajectories in $BaZr_{0.875}Y_{0.125}O_3$ due to the presence of other protons. J. Korean Ceram. Soc. **53**(5), 521–528 (2016)
17. J. Mizusaki, M. Yoshihiro, S. Yamauchi, K. Fueki, Nonstoichiometry and defect structure of the perovskite-type oxides $La_{1-x}Sr_xFeO_{3-}$. J. Solid State Chem. **58**(2), 257–266 (1985)
18. T. Mayeshiba, D. Morgan, Strain effects on oxygen vacancy formation energy in perovskites. Solid State Ionics **311**, 105–117 (2017)
19. D.A. Kuznetsov, B. Han, Y. Yu, R.R. Rao, J. Hwang, Y. Román-Leshkov, Y. Shao-Horn, Tuning redox transitions via inductive effect in metal oxides and complexes, and implications in oxygen electrocatalysis. Joule **2**(2), 225–244 (2018)
20. L. Sun, H. Qin, K. Wang, M. Zhao, J. Hu, Structure and electrical properties of nanocrystalline $La_{1-x}Ba_xFeO_3$ for Gas Sensing Application. Mater. Chem. Phys. **125**(1-2), 305–308 (2011)
21. J. Zhang, C. Zhang, W. Li, Q. Guo, H. Gao, Y. You, Y. Li, Z. Cui, K.C. Jiang, H. Long, Nitrogen-doped perovskite as a bifunctional cathode catalyst for rechargeable lithium-oxygen batteries. ACS Appl. Mater. Interfaces. **10**(6), 5543–5550 (2018)
22. W.J. Yin, B. Weng, J. Ge, Q. Sun, Z. Li, Y. Yan, Oxide perovskites, double perovskites and derivatives for electrocatalysis, photocatalysis, and photovoltaics. Energy Environ. Sci. **12**(2), 442–462 (2019)
23. M.L. Post, J.J. Tunney, D. Yang, X. Du, D.L. Singleton, Material chemistry of perovskite compounds as chemical sensors. Sens. Actuators B **59**(2-3), 190–194 (1999)
24. S.S. Shin, E.J. Yeom, W.S. Yang, S. Hur, M.G. Kim, J. Im, J. Seo, J.H. Noh, S.I. Seok, Colloidally prepared La-doped $BaSnO_3$ electrodes for efficient, photostable perovskite solar cells. Science **356**(6334), 167–171 (2017)
25. H.U. Anderson, Review of *P*-type doped perovskite materials for SOFC and other applications. Solid State Ionics **52**(1-3), 33–41 (1992)
26. H. Obayashi, Y. Sakurai, T. Gejo, Perovskite-Type Oxides as Ethanol Sensors. J. Solid State Chem. **17**(3), 299–303 (1976)
27. T. Seiyama, N. Yamazoe, K. Eguchi, Characterization and activity of some mixed metal oxide catalysts. Ind. Eng. Chem. Prod. Res. Dev. **24**(1), 19–27 (1985)
28. S. Thirumalairajan, K. Girija, V.R. Mastelaro, N. Ponpandian, Surface morphology-dependent room-temperature $LaFeO_3$ nanostructure thin films as selective NO_2 gas sensor prepared by radio frequency magnetron sputtering. ACS Appl. Mater. Interfaces. **6**(16), 13917–13927 (2014)
29. A. Queraltó, D. Graf, R. Frohnhoven, T. Fischer, H. Vanrompay, S. Bals, A. Bartasyte, S. Mathur, $LaFeO_3$ nanofibers for high detection of sulfur-containing gases. ACS Sustain Chem. Eng. **7**(6), 6023–6032 (2019)
30. Y. Shimizu, M. Shimabukuro, H. Arai, T. Seiyama, Enhancement of humidity sensitivity for perovskite-type oxides having semiconductivity. Chem. Lett. **14**(7), 917–920 (1985)
31. X.L. Yu, Y. Wang, Y.M. Hu, C.B. Cao, H.L.W. Chan, Gas-sensing properties of perovskite BifeO3 nanoparticles. J. Am. Ceram. Soc. **92**(12), 3105–3107 (2009)
32. H.T. Fan, X.J. Xu, X.K. Ma, T. Zhang, Preparation of $LaFeO_3$ nanofibers by electrospinning for gas sensors with fast response and recovery. Nanotechnology **22**(11), 115502 (2011)
33. P. Song, Q. Wang, Z. Zhang, Z. Yang, Synthesis and gas sensing properties of biomorphic $LaFeO_3$ hollow fibers templated from cotton. Sens. Actuators B **147**(1), 248–254 (2010)
34. M.C. Carotta, M.A. Butturi, G. Martinelli, Y. Sadaoka, P. Nunziante, E. Traversa, Microstructural evolution of nanosized $LaFeO_3$ powders from the thermal decomposition of a cyano-complex for thick film gas sensors. Sens. Actuators B **44**(1-3), 590–594 (1997)
35. H. Xiao, C. Xue, P. Song, J. Li, Q. Wang, Preparation of porous $LaFeO_3$ microspheres and their gas-sensing property. Appl. Surf. Sci. **337**, 65–71 (2015)
36. D. Wang, X. Chu, M. Gong, Single-Crystalline $LaFeO_3$ Nanotubes with Rough Tube Walls: Synthesis and Gas-Sensing Properties. Nanotechnology **17**(21), 5501 (2006)
37. M. Fleischer, S. Kornely, T. Weh, J. Frank, H. Meixner, Selective gas detection with high-temperature operated metal oxides using catalytic filters. Sens. Actuators B **69**(1-2), 205–210 (2000)
38. J.W. Yoon, J.S. Kim, T.H. Kim, Y.J. Hong, Y.C. Kang, J.H. Lee, A new strategy for humidity independent oxide chemiresistors: dynamic self-refreshing of $In2O_3$ sensing surface assisted by

layer-by-layer coated CeO_2 nanoclusters. Small **12**(31), 4229–4240 (2016)
39. H.Y. Li, C.S. Lee, D.H. Kim, J.H. Lee, Flexible room-temperature NH_3 sensor for ultrasensitive, selective, and humidity-independent gas detection. ACS Appl. Mater. Interfaces. **10**(33), 27858–27867 (2018)
40. X.H. Ma, H.Y. Li, S.H. Kweon, S.Y. Jeong, J.H. Lee, S. Nahm, Highly sensitive and selective $PbTiO_3$ gas sensors with negligible humidity interference in ambient atmosphere. ACS Appl. Mater. Interfaces. **11**(5), 5240–5246 (2019)
41. T. Ishihara, H. Matsuda, Y. Takita, Doped $LaGaO_3$ perovskite type oxide as a new oxide ionic conductor. J. Am. Chem. Soc. **116**(9), 3801–3803 (1994)
42. S. Palimar, S. Kaushik, V. Siruguri, D. Swain, A.E. Viegas, C. Narayana, N.G. Sundaram, Investigation of Ca substitution on the gas sensing potential of $LaFeO_3$ nanoparticles towards low concentration SO_2 gas. Dalton Trans. **45**(34), 13547–13555 (2016)
43. A.A. Ansari, N. Ahmad, M. Alam, S.F. Adil, S.M. Ramay, A. Albadri, A. Ahmad, A.M. Al-Enizi, B.F. Alrayes, M.E. Assal, Physico-chemical properties and catalytic activity of the sol-gel prepared ce-ion doped $LaMnO_3$ perovskites. Sci. Rep. **9**(1), 7747 (2019)
44. P.A. Murade, V.S. Sangawar, G.N. Chaudhari, V.D. Kapse, A.U. Bajpeyee, Acetone gas-sensing performance of sr-doped nanostructured LaFeO-3 semiconductor prepared by citrate sol–gel route. Curr. Appl. Phys. **11**(3), 451–456 (2011)
45. K. Fan, H. Qin, L. Wang, L. Ju, J. Hu, CO_2 gas sensors based on $La_{1-x}Sr_xFeO_3$ nanocrystalline powders. Sens. Actuators B **177**, 265–269 (2013)
46. L. Zhou, X. Li, H. Wu, Z. Liao, Q. Yuan, F. Xia, J. Xiao, Sensing properties of YSZ-based NO_x sensors with double-perovskite $(La_{0.8}Sr_{0.2})$ $2FeNiO_{6-\delta}$-sensing electrodes. Ceram. Int. **40**(7), 9257–9263 (2014)
47. L.B. Kong, Y.S. Shen, Gas-sensing property and mechanism of $Ca_xLa_{1-x}FeO_3$ ceramics. Sens. Actuators B **30**(3), 217–221 (1996)
48. J. Qin, Z. Cui, X. Yang, S. Zhu, Z. Li, Y. Liang, Three-dimensionally ordered macroporous $La_{1-x}Mg_xFeO_3$ as high performance gas sensor to methanol. J. Alloys Compd. **635**, 194–202 (2015)
49. V. Lantto, S. Saukko, N.N. Toan, L.F. Reyes, C.G. Granqvist, Gas sensing with perovskite-like oxides having ABO_3 and BO_3 structures. J. Electroceram. **13**(1-3), 721–726 (2004)
50. M. Bektas, D. Schönauer-Kamin, G. Hagen, A. Mergner, C. Bojer, S. Lippert, W. Milius, J. Breu, R. Moos, $BaFe_{1-x}Ta_xO_{3-\delta}$—a material for temperature independent resistive oxygen sensors. Sens. Actuators B **190**, 208–213 (2014)
51. J. Gerblinger, M. Hausner, H. Meixner, Electric and kinetic properties of screen-printed strontium titanate films at high temperatures. J. Am. Ceram. Soc. **78**(6), 1451–1456 (1995)
52. F. Rettig, R. Moos, C. Plog, Poisoning of temperature independent resistive oxygen sensors by sulfur dioxide. J. Electroceram. **13**(1-3), 733–738 (2004)
53. P.M. Bulemo, J. Lee, I.D. Kim, Heterogeneous porous WO_3@ SnO_2 nanofibers as gas sensing layers for chemiresistive sensory devices. J. Sens. Sci. Technol. **27**(5), 345–351 (2018)
54. A. Sharma, M. Tomar, V. Gupta, Low temperature operating SnO_2 thin film sensor loaded with WO_3 micro-discs with enhanced response for NO_2 gas. Sens. Actuators B **161**(1), 1114–1118 (2012)
55. Y. Gui, F. Dong, Y. Zhang, Y. Zhang, J. Tian, Preparation and gas sensitivity of WO_3 hollow microspheres and SnO_2 doped heterojunction sensors. Mater. Sci. Semicond. Process. **16**(6), 1531–1537 (2013)
56. T.S. Wang, Q.S. Wang, C.L. Zhu, Q.Y. Ouyang, L.H. Qi, C.Y. Li, G. Xiao, P. Gao, Y.J. Chen, Synthesis and enhanced H_2S gas sensing properties of α-MoO_3/CuO *p–n* junction nanocomposite. Sens. Actuators B **171**, 256–262 (2012)
57. Z.U. Abideen, J.H. Kim, J.H. Lee, J.Y. Kim, A. Mirzaei, H.W. Kim, S.S. Kim, Electrospun metal oxide composite nanofibers gas sensors: a review. J. Korean Ceram. Soc. **54**(5), 366–379 (2017)
58. S. Joshi, F. Antolasic, M.V. Sunkara, S.K. Bhargava, S.J. Ippolito, Highly selective CO_2 gas sensing properties of CaO–$BaTiO_3$ heterostructures effectuated through discretely created *n–n* nanointerfaces. ACS Sustain Chem. Eng. **6**(3), 4086–4097 (2018)
59. Y. Wang, Y. Zhu, S. Wu, A new nano CaO-based CO_2 adsorbent prepared using an adsorption phase technique. Chem. Eng. J. **218**, 39–45 (2013)
60. N. Zhang, S. Ruan, Y. Yin, F. Li, S. Wen, Y. Chen, Self-sacrificial template-driven $LaFeO_3$/α-Fe2O_3 porous nano-octahedrons for acetone sensing. ACS Appl. Nano Mater. **1**(9), 4671–4681 (2018)
61. Q. Peng, J. Wang, Z. Feng, C. Du, Y. Wen, B. Shan, R. Chen, Enhanced photoelectrochemical water oxidation by fabrication of *p*-$LaFeO_3$/*n*-Fe_2O_3 heterojunction on hematite nanorods. J. Phys. Chem. C **121**(24), 12991–12998 (2017)
62. W. Wei, S. Guo, C. Chen, L. Sun, Y. Chen, W. Guo, S. Ruan, High sensitive and fast formaldehyde gas sensor based on Ag-doped $LaFeO_3$ nanofibers. J. Alloys Compd. **695**, 1122–1127 (2017)
63. Y.M. Zhang, Y.T. Lin, J.L. Chen, J. Zhang, Z.Q. Zhu, Q.J. Liu, A high sensitivity gas sensor for formaldehyde based on silver doped lanthanum ferrite. Sens. Actuators B **190**, 171–176 (2014)
64. S. Joshi, S.J. Ippolito, S. Periasamy, Y.M. Sabri, M.V. Sunkara, Efficient heterostructures of Ag@CuO/$BaTiO_3$ for low-temperature CO-$_2$ Gas detection: assessing the role of nanointerfaces during sensing by operando DRIFTS technique. ACS Appl. Mater. Interfaces. **9**(32), 27014–27026 (2017)
65. H. Zhang, H. Qin, P. Zhang, J. Hu, High sensing properties of 3 Wt% Pd-doped $SmFe_{1-x}Mg_xO_3$ nanocrystalline powders to acetone vapor with ultralow concentrations under light illumination. ACS Appl. Mater. Interfaces. **10**(18), 15558–15564 (2018)
66. L. Dai, L. Ma, W. Meng, Y. Li, Z. He, L. Wang, Impedancemetric NO_2 sensor based on Pd doped perovskite oxide sensing electrode conjunction with phase angle response. Electrochim. Acta **265**, 411–418 (2018)
67. E. Cao, A. Wu, H. Wang, Y. Zhang, W. Hao, L. Sun, Enhanced ethanol sensing performance of Au and Cl comodified $LaFeO_3$ nanoparticles. ACS Appl. Nano Mater. **2**(3), 1541–1551 (2019)
68. J. Suntivich, H.A. Gasteiger, N. Yabuuchi, H. Nakanishi, J.B. Goodenough, Y. Shao-Horn, Design principles for oxygen-reduction activity on perovskite oxide catalysts for fuel cells and metal–air batteries. Nat. Chem. **3**(7), 546 (2011)
69. C.H. Kim, G. Qi, K. Dahlberg, W. Li, Strontium-doped perovskites rival platinum catalysts for treating NO_x in simulated diesel exhaust. Science **327**(5973), 1624–1627 (2010)
70. B.P. Barbero, J.A. Gamboa, L.E. Cadús, Synthesis and characterisation of $La_{1-x}Ca_xFeO_3$ perovskite-type oxide catalysts for total oxidation of volatile organic compounds. Appl. Catal. B **65**(1–2), 21–30 (2006)
71. J. Zhu, A. Thomas, Perovskite-type mixed oxides as catalytic material for NO removal. Appl. Catal. B **92**(3–4), 225–233 (2009)
72. Z. Du, P. Yang, L. Wang, Y. Lu, J.B. Goodenough, J. Zhang, D. Zhang, Electrocatalytic performances of $LaNi_{1-x}Mg_xO_3$ perovskite oxides as bi-functional catalysts for lithium air batteries. J. Power Sour **265**, 91–96 (2014)
73. D.W. Hwang, H.G. Kim, J. Kim, K.Y. Cha, Y.G. Kim, J.S. Lee, Photocatalytic water splitting over highly donor-doped (110) layered perovskites. J. Catal. **193**(1), 40–48 (2000)

74. H. Zhang, J. Yi, Enhanced ethanol gas sensing performance of ZnO nanoflowers decorated with $LaMnO_3$ perovskite nanoparticles. Mater. Lett. **216**, 196–198 (2018)
75. H.J. Lin, J.P. Baltrus, H. Gao, Y. Ding, C.Y. Nam, P. Ohodnicki, P.X. Gao, Perovskite nanoparticle-sensitized Ga_2O_3 nanorod arrays for CO detection at high temperature. ACS Appl. Mater. Interfaces. **8**(14), 8880–8887 (2016)
76. J.Y. Kang, J.S. Jang, W.T. Koo, J. Seo, Y. Choi, M.H. Kim, D.H. Kim, H.J. Cho, W. Jung, I.D. Kim, Perovskite $La_{0.75}Sr_{0.25}Cr_{0.5}Mn_{0.5}O_{3-\delta}$ sensitized SnO_2 fiber-in-tube scaffold: highly selective and sensitive formaldehyde sensing. J. Mater. Chem. A **6**(22), 10543–10551 (2018)
77. N. Yamazoe, Y. Kurokawa, T. Seiyama, Effects of additives on semiconductor gas sensors. Sens. Actuators **4**, 283–289 (1983)
78. J.S. Jang, S.J. Choi, S.J. Kim, M. Hakim, I.D. Kim, Rational design of highly porous SnO_2 nanotubes functionalized with biomimetic nanocatalysts for direct observation of simulated diabetes. Adv. Funct. Mater. **26**(26), 4740–4748 (2016)
79. G. Sakai, N. Matsunaga, K. Shimanoe, N. Yamazoe, Theory of gas-diffusion controlled sensitivity for thin film semiconductor gas sensor. Sens. Actuators B **80**(2), 125–131 (2001)
80. S.J. Kim, S.J. Choi, J.S. Jang, N.H. Kim, M. Hakim, H.L. Tuller, I.D. Kim, Mesoporous WO_3 nanofibers with protein-templated nanoscale catalysts for detection of trace biomarkers in exhaled breath. ACS Nano **10**(6), 5891–5899 (2016)
81. K.H. Kim, S.J. Kim, H.J. Cho, N.H. Kim, J.S. Jang, S.J. Choi, I.D. Kim, WO_3 nanofibers functionalized by protein-templated RuO_2 nanoparticles as highly sensitive exhaled breath gas sensing layers. Sens. Actuators B **241**, 1276–1282 (2017)
82. Y.J. Jeong, W.T. Koo, J.S. Jang, D.H. Kim, H.J. Cho, I.D. Kim, Chitosan-templated Pt nanocatalyst loaded mesoporous SnO_2 nanofibers: a superior chemiresistor toward acetone molecules. Nanoscale **10**(28), 13713–13721 (2018)
83. Y. Li, X. Zhou, W. Luo, X. Cheng, Y. Zhu, A.M. El-Toni, A. Khan, Y. Deng, D. Zhao, Pore engineering of mesoporous tungsten oxides for ultrasensitive gas sensing. Adv. Mater. Interfaces **6**(1), 1801269 (2019)
84. V.K. Tomer, S. Duhan, Ordered mesoporous Ag-Doped TiO_2/SnO_2 nanocomposite based highly sensitive and selective VOC sensors. J. Mater. Chem. A **4**(3), 1033–1043 (2016)
85. R. Malik, V.K. Tomer, L. Kienle, V. Chaudhary, S. Nehra, S. Duhan, Ordered mesoporous Ag–ZnO@ g-CN nanohybrid as highly efficient bifunctional sensing material. Adv. Mater. Interfaces **5**(8), 1701357 (2018)
86. P.M. Bulemo, H.J. Cho, D.H. Kim, I.D. Kim, Facile synthesis of Pt-functionalized meso/macroporous SnO_2 hollow spheres through in situ templating with SiO_2 for H_2S sensors. ACS Appl. Mater. Interfaces. **10**(21), 18183–18191 (2018)
87. S.J. Choi, C. Choi, S.J. Kim, H.J. Cho, M. Hakim, S. Jeon, I.D. Kim, Highly efficient electronic sensitization of non-oxidized graphene flakes on controlled pore-loaded WO_3 nanofibers for selective detection of H_2S molecules. Sci. Rep. **5**, 8067 (2015)
88. T. Wang, I. Can, S. Zhang, J. He, P. Sun, F. Liu, G. Lu, Self-assembly template driven 3D inverse opal microspheres functionalized with catalyst nanoparticles enabling a highly efficient chemical sensing platform. ACS Appl. Mater. Interfaces. **10**(6), 5835–5844 (2018)
89. M.C. Chang, Three dimensionally ordered microstructure of polycrystalline TiO_2 ceramics with micro/meso porosity. J. Korean Ceram. Soc. **53**(2), 227–233 (2016)
90. M.C. Chang, Three dimensionally ordered microstructure of polycrystalline zirconia ceramics with micro-porosity. J. Korean Ceram. Soc. **53**(1), 50–55 (2016)
91. P. Song, Q. Wang, Z. Yang, CO-sensing characteristics of La0.8Pb0.2Fe0.8Co0.2O3 perovskite films prepared by RF magnetron sputtering. Phys E (Amst. Neth.) **41**(8), 1479–1483 (2009)
92. L. Ma, S.Y. Ma, X.F. Shen, T.T. Wang, X.H. Jiang, Q. Chen, Z. Qiang, H.M. Yang, H. Chen, $PrFeO_3$ hollow nanofibers as a highly efficient gas sensor for acetone detection. Sens. Actuators B **255**, 2546–2554 (2018)
93. D. Chen, J. Yi, One-pot electrospinning and gas-sensing properties of $LaMnO_3$ perovskite/SnO_2 heterojunction nanofibers. J. Nanopart. Res. **20**(3), 65 (2018)
94. Y. Zhang, Z. Duan, H. Zou, M. Ma, Fabrication of electrospun $LaFeO_3$ nanotubes via annealing technique for fast ethanol detection. Mater. Lett. **215**, 58–61 (2018)
95. B. Wang, Q. Yu, S. Zhang, T. Wang, P. Sun, X. Chuai, G. Lu, Gas sensing with yolk-shell $LafeO_3$ microspheres prepared by facile hydrothermal synthesis. Sens. Actuators B **258**, 1215–1222 (2018)
96. Z. Dai, C.S. Lee, B.Y. Kim, C.H. Kwak, J.W. Yoon, H.M. Jeong, J.H. Lee, Honeycomb-like periodic porous $LaFeO_3$ thin film chemiresistors with enhanced gas-sensing performances. ACS Appl. Mater. Interfaces. **6**(18), 16217–16226 (2014)
97. M. Chen, H. Wang, J. Hu, Y. Zhang, K. Li, D. Zhang, S. Zhou, J. Zhang, Z. Zhu, Q. Liu, Near-room-temperature ethanol gas sensor based on mesoporous Ag/Zn–LaFeO3 nanocomposite. Adv. Mater. Interfaces **6**(1), 1801453 (2019)
98. P.M. Bulemo, H.J. Cho, N.H. Kim, I.D. Kim, Mesoporous SnO_2 nanotubes via electrospinning-etching route: highly sensitive and selective detection of H_2S molecule. ACS Appl. Mater. Interfaces. **9**(31), 26304–26313 (2017)
99. T. Zhou, T. Zhang, R. Zhang, Z. Lou, J. Deng, G. Lu, L. Wang, Constructing *P–N* heterostructures for efficient structure-driven ethanol sensing performance. Sens. Actuators B **255**, 745–753 (2018)
100. P. Song, H. Zhang, D. Han, J. Li, Z. Yang, Q. Wang, Preparation of biomorphic porous $LaFeO_3$ by sorghum straw biotemplate method and its acetone sensing properties. Sens. Actuators B **196**, 140–146 (2014)
101. W.M. Xu, K. Chai, Y.W. Jiang, J. Mao, J. Wang, P. Zhang, Y. Shi, 2D Single Crystal WSe_2 and $MoSe_2$ nanomeshes with quantifiable high exposure of layer edges from 3D mesoporous silica template. ACS Appl. Mater. Interfaces **11**(19), 17670–17677 (2019)
102. S.J. Choi, I.D. Kim, Recent developments in 2D nanomaterials for chemiresistive-type gas sensors. Electron. Mater. Lett. **14**(3), 221–260 (2018)
103. D. Zappa, V. Galstyan, N. Kaur, H. M. M. Arachchige, O. Sisman, E. Comini, "Metal oxide-based heterostructures for gas sensors"—a review. Anal. Chim. Acta. **1039**, 1–23 (2018)
104. M. Chen, Y. Zhang, J. Zhang, K. Li, T. Lv, K. Shen, Z. Zhu, Q. Liu, Facile lotus-leaf-templated synthesis and enhanced xylene gas sensing properties of Ag-$LaFeO_3$ nanoparticles. J. Mater. Chem. C **6**(23), 6138–6145 (2018)
105. A. Bala, S. Majumder, M. Dewan, A.R. Chaudhuri, Hydrogen sensing characteristics of perovskite based calcium doped $BiFeO_3$ thin films. Int J Hydrogen Energ **44**(33), 18648–18656 (2019)